

Towards Human-Level 3D Relative Pose Estimation: Generalizable, Training-Free, with Single Reference

Yuan Gao*, Yajing Luo*, Junhong Wang, Kui Jia, Gui-Song Xia

Abstract—Humans can easily deduce the relative pose of a previously unseen object, without labeling or training, given only a single query-reference image pair. This is arguably achieved by incorporating (i) 3D/2.5D shape perception from a single image, (ii) render-and-compare simulation, and (iii) rich semantic cue awareness to furnish (coarse) reference-query correspondence. Existing methods implement (i) by a 3D CAD model or well-calibrated multiple images and (ii) by training a network on specific objects, which necessitate laborious ground-truth labeling and tedious training, potentially leading to challenges in generalization. Moreover, (iii) was less exploited in the paradigm of (ii), despite that the coarse correspondence from (iii) is able to enhance the compare process by filtering out non-overlapped parts under substantial pose differences/occlusions. Motivated by this, we propose a novel 3D generalizable relative pose estimation method by elaborating (i) with a 2.5D shape from an RGB-D reference, (ii) with an off-the-shelf differentiable renderer, and (iii) with semantic cues from a pretrained model like DINOv2. Specifically, our differentiable renderer takes the 2.5D rotatable mesh textured by the RGB and the semantic maps (obtained by DINOv2 from the RGB input), then renders new RGB and semantic maps (with back-surface culling) under a novel rotated view. The refinement loss comes from comparing the rendered RGB and semantic maps with the query ones, back-propagating the gradients through the differentiable renderer to refine the 3D relative pose. As a result, *our method can be readily applied to unseen objects, given only a single RGB-D reference, without labeling or training*. Extensive experiments on LineMOD, LM-O, and YCB-V show that our training-free method significantly outperforms the state-of-the-art supervised methods, especially under the rigorous $\text{Acc}@5/10/15^\circ$ metrics and the challenging cross-dataset settings. The codes are available at https://github.com/ethanygao/training-free_generalizable_relative_pose.

Index Terms—3D Relative Pose Estimation, Differentiable Renderer, Zero-Shot Unseen Generalization, Single Reference, Label/Training-Free Refinement.

I. INTRODUCTION

RECENT years have witnessed great progress in 3D object pose estimation [20, 40, 42, 63, 66, 76, 77], which estimates the 3D rotation of an object depicted in a query RGB image. As a key to facilitating interaction with real-world objects, 3D object pose estimation attracts increasing

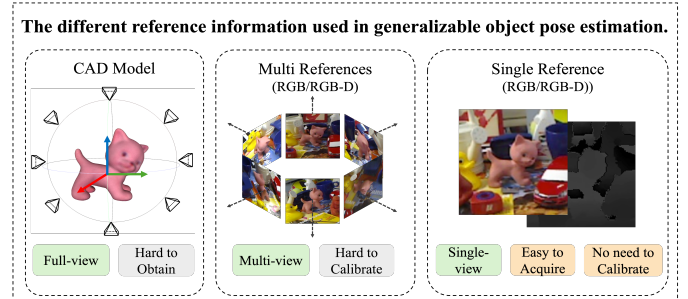


Fig. 1. Generalizable object pose estimation with different references, i.e., a CAD model, multiple images, or a single image. CAD models and multi-view references offer rich geometry details, however, scanning the precise CAD model and/or calibrating dense views for multiple images are laborious or even impossible for unseen objects in practice, such as augmented reality. We thus focus on estimating the relative pose w.r.t. a single-view reference following [76, 77], i.e., the relative pose between a reference-query pair, where we treat the reference pose as canonical without any calibration.

attention from various areas including computer vision, virtual/augmented reality, robotics, and human-computer interaction [1, 48, 58]. To date, the community shows great interest in generalizable 3D object pose estimation [15, 42, 57, 75, 76, 77] owing to its wide applicability, which focuses on the generalization to previously unseen objects, preferably in a zero-shot manner¹.

Existing generalizable 3D object pose estimation methods can be categorized according to how they exploit the reference information, i.e., using a CAD model, multiple images, or a single image as references, as shown in Fig. 1. Specifically, most existing methods leverage a 3D CAD model [8, 24, 42, 43, 54] or multiple images [15, 17, 32, 38, 46, 57, 75] for template matching or feature extraction, while the requirement of laborious 3D scanning (for the CAD-based methods) or multiple-image pose labeling (for most multi-image methods) severely limits their applicability.

On the other hand, recent methods propose to reframe the generalizable object pose estimation task as relative pose estimation between a query and a reference images from an unseen object, which is termed as *generalizable relative object pose estimation* [76, 77]. By treating the reference pose as canonical, estimating the relative pose between the reference-query pair successfully bypasses the laborious 3D scanning (of the CAD reference) or dense views calibration (of the multiple-image reference). However, existing methods rely on a large amount of well-labeled poses between the query-reference pairs to effectively train a neural network, thereby imposing the challenge of acquiring high-quantity

¹We discuss the relatively easier instance- or category-level object pose estimation in the Related Work Sect. II-A and II-B, respectively.

Y. Gao is with the School of Electronic Information, Wuhan University, Wuhan, China. E-mail: ethan.y.gao@gmail.com

Y. Luo and G.-S. Xia are with the School of Computer Science, Wuhan University, Wuhan, China. E-mails: {yajingluo, guisong.xia}@whu.edu.cn

J. Wang is with MoreFun Studio, Tencent Games, Tencent, Shenzhen, China. E-mails: junhongwang@tencent.com

K. Jia is with the School of Data Science, The Chinese University of Hong Kong, Shenzhen, China. E-mails: kuijia@cuhk.edu.cn

Corresponding authors: Gui-Song Xia, Yuan Gao.

* indicates equal contribution.

TABLE I

THE TAXONOMY OF OUR METHOD IN **GENERALIZABLE POSE ESTIMATION**. FOR EACH COLUMN, WE ILLUSTRATE THE APPLICABILITY IN DESCENDING ORDER USING THE TEXT OF **BOLD**, UNDERLINED, AND NORMAL. WE ALSO INCLUDE THE HUMAN INTELLIGENCE AS A REFERENCE. THE STATE-OF-THE-ART METHODS USED IN OUR EXPERIMENTS ARE HIGHLIGHTED WITH THEIR NAME.

Method	Training	Label	Reference		Query	
			Modality	#Instance	Modality	#Instance
Human Intelligence	training-free	label-free	RGB	single	RGB	single
[8, 33, 43]	supervised	<u>pose</u>	CAD	multiple	RGB-D	single
[24, 41, 42, 45, 54]	supervised	<u>pose</u>	CAD	multiple	RGB	single
[17, 46]	supervised	<u>pose</u>	<u>RGB-D</u>	multiple	RGB-D	single
RelPose++ [32], [15, 38, 57, 75]	supervised	<u>pose</u>	RGB	multiple	RGB	single
LoFTR [56]	supervised	pose+depth	RGB	single	RGB	single
3DAHV [77], DVMNet [76]	supervised	<u>pose</u>	RGB	single	RGB	single
ZSP [14]	training-free	label-free	<u>RGB-D</u>	single	RGB-D	multiple
Ours	training-free	label-free	<u>RGB-D</u>	single	RGB	single

training data [32, 75, 76, 77]. Moreover, the generalizability of some network-based methods may be hindered by the training datasets. We empirically find that after pretrained on an external large-scale dataset such as Objaverse [11], the current state-of-the-art methods [76, 77] need to perform in-dataset finetune² before testing on the in-dataset unseen objects, which impedes the cross-dataset generalize-ability.

In this context, we work towards universally applicable zero-shot 3D generalizable relative pose estimation, where (i) the object is agnostic/unseen from a cross-dataset, (ii) only a single RGB-D image is available for reference without a 3D CAD model or multi-view images, and (iii) the ground-truth (relative) pose label is not available. In other words, we aim to establish a novel 3D generalizable (in terms of both objects and datasets) relative pose estimation method given only one reference and one query image, without labeling or training. This is extremely challenging due to the mixture of **incomplete shape information** and **missing reference-query correspondence**, which leads to a severely degraded optimization problem.

Our method is inspired by the fact that humans can easily infer the relative pose under the aforementioned rigorous setting, even with large pose differences or severe occlusions. We hypothesize that such intelligence is accomplished through (i) perceiving 3D/2.5D shapes from a single image, (ii) conducting render-and-compare simulations via imagination, and (iii) understanding rich semantic cues of the object. For example, given two viewpoints of an unseen animal, humans are able to infer the 3D/2.5D shape of that animal, then identify the correspondences of the animal eyes, noses, ears, etc, and finally rotate and render the 3D/2.5D model until its projection matches the other view. Note that the semantic cues have the potential to deal with the (self-) occluded missing parts, thus enhancing the comparison process, e.g., an animal tail can be simply ignored in the render-and-compare simulations if it only appears in one image and is (self-) occluded in the other.

The above analysis motivates us to break down our difficulties and fulfill those three requirements. Concretely, we achieve this by formulating a label/training-free framework through an off-the-shelf differentiable renderer following the

render-and-compare paradigm. Our input shape to the differentiable renderer is an RGB- and semantic-textured 2.5D mesh of the reference (avoiding the difficult 3D hallucination of an unseen object). Based on this, we construct a pose refinement framework, where the differentiable renderer takes an initial pose to render projections, then back-propagates the gradients from the projection loss (between the rendered and the query images) to refine the initial pose.

Specifically, our method starts with an RGB-D reference and an RGB query, where their semantic maps can be obtained by leveraging an advanced pretrained model DINOv2 [44] with the RGB inputs³. We leverage an easy-to-use differentiable renderer nvdiffrast [25], which takes the RGB- and semantic-textured 2.5D mesh of the reference as input, then renders new RGB and semantic maps (with back-surface culling) under a novel rotated view. The pose refinement loss comes from comparing the rendered RGB and semantic maps with the query ones, which flows the gradients through the differentiable renderer to refine the 3D relative pose. As a result, our method can be readily applied to unseen objects from an arbitrary dataset without labeling or training.

In summary, we propose a novel 3D generalizable relative pose estimation method, which takes only an RGB-D reference and an RGB query pair, without requiring the ground-truth pose labels or training. We achieve this by formulating a pose refinement framework via an off-the-shelf differentiable renderer under the render-and-compare paradigm. Our method does not involve training a network, which naturally possesses zero-shot generalize-ability in terms of both unseen objects and datasets. We conducted extensive experiments on LineMOD [18], LM-O [3] and YCB-V [69] datasets. The results from our training-free method exhibit significant improvement over the state-of-the-art supervised methods, e.g., for $\text{Acc}@15^\circ$ metric on the LineMOD dataset [18] and the YCB-V dataset [69], our label- and training-free method outperforms the supervised state-of-the-art results by **29.98%** and **14.28%**, respectively.

³Note that our method possesses the potential of using only an RGB reference, please see the discussion in Sect. I-A (Applicability) and Sect. VI (Limitations and Future Works) for more details. Moreover, our method works reasonably well even without the DINOv2 semantic maps on the LineMOD dataset, as illustrated in Table V.

²The in-dataset finetuning denotes that the finetune set comes from the same dataset with the testing set, while not including the testing objects.

A. Taxonomy and Applicability of Our Method

Taxonomy. The taxonomy of our methods in generalizable pose estimation, in terms of training, labeling, as well as the modality and the number of required instances of the *reference* and the *query* images, is illustrated in Table I. Our method falls under the category of *label/training-free* with a *single RGB query* and a *single RGB-D reference*.

Applicability. Among Table I, the proposed method shares the closest setting to the human intelligence on relative pose estimation that is able to generalize to unseen objects from an arbitrary dataset, with only an additional one-time-collection depth map for the reference image. We have testified in supplementary material that our method can still deliver good estimations with an imprecise depth map, which implies the potential to fully distill human intelligence by a generalizable depth estimator. We note that training a generalizable depth estimator is beyond the scope of, and may introduce distractions to, our current focus. In addition, our method also incorporates the segmentation maps of both query and reference objects as input, which can be obtained by pretrained segmentation models such as SAM [23], FastSAM [79] and Grounded SAM [52]. We chose not to delve into these segmentation techniques extensively either, for the same sake of minimizing potential distractions.

II. RELATED WORK

A. Instance-level 6D Pose Estimation

Current object pose estimation can be categorized into instance-level, category-level, and generalizable methods based on different problem formulations. For instance-level methods, there are roughly three categories: direct regression-based, correspondence-based, and refinement-based. Direct regression-based methods [4, 21, 49, 59, 69] predict the object pose directly through a neural network. Correspondence-based methods [12, 16, 19, 30, 31, 47, 55, 64, 71, 73] estimate the 2D-3D/3D-3D correspondence between the 2D images and 3D object models, followed by PnP solvers [28] to calculate 6D poses. Additionally, refinement-based methods [29, 37, 70] incorporate refinement-based steps to improve the prediction performance. However, instance-level methods are trained on instance-specific data and rely heavily on CAD models to render numerous training data. Consequently, their application is limited to the objects on which they were trained.

B. Category-level 6D Pose Estimation

In category-level methods, the test instances are not seen during training but belong to known categories. Most methods achieve this by either alignment or directly regressing. Alignment-based methods [9, 27, 34, 60, 62, 65] first propose a Normalized Object Coordinate Space (NOCS) [65] as a canonical representation for all possible object instances within a category. A network is then trained to predict the NOCS maps and align the object point cloud with the NOCS maps using the Umeyama algorithm [61] to determine the object pose. This method typically constructs the mean shape of specific categories as shape priors using offline categorical object models,

and the networks are trained to learn deformation fields from the shape priors to enhance the prediction of NOCS maps. In contrast, directly regressing methods [7, 10, 35, 36, 39] avoid the non-differentiable Umeyama algorithm and often focus on geometry-aware feature extraction. For instance, CASS [7] contrasts and fuses shape-dependent/pose-dependent features to predict both the object’s pose and size directly. Fs-net [10] leverages 3D Graph Convolution for latent feature extraction, and designs shape-based and residual-based networks for pose estimation. However, while category-level methods strive to address different instances within the same category, their capacity to predict the poses of objects from entirely new categories remains limited, highlighting the ongoing need to broaden the scope of object pose estimation to encompass unfamiliar objects.

C. Generalizable 6D Pose Estimation

Generalizable algorithms aim to enhance the generalizability of unseen objects without the need for retraining or finetuning. Methods in this category can be classified as CAD-based [5, 8, 24, 41, 42, 43, 45, 54] or multi-view reference-based [15, 17, 38, 46, 57, 67].

For CAD-based approaches, CAD models are often used as prior knowledge for direct feature matching or template generation. In particular, ZeroPose [8] performs point feature extraction for both CAD models and observed point clouds, utilizing a hierarchical geometric feature matching network to establish correspondences. Following ZeroPose, SAM-6D [33] proposed a two-stage partial-to-partial point matching model to construct dense 3D-3D correspondence effectively. Instead, Template-Pose [42] utilizes a CAD model to generate a collection of templates and selects the most similar one for a given query image. Similarly, OSOP [54] renders plenty of templates and estimates the 2D-2D correspondence between the best matching template and the query image to solve the object pose. MegaPose [24] proposed a coarse network to classify which rendered image best matches the query image and generate an initial pose. Subsequently, multi-view renderings of the initial pose are produced, and a refiner is trained to predict an updated pose.

Multi-view reference-based methods can be further divided into feature matching-based and template matching-based approaches. For the former, multi-view reference-based feature matching methods mainly aim to establish 2D-3D correspondences between the RGB query image and sparse point cloud reconstructed by reference views or 3D-3D correspondences between the RGB-D query and RGB-D reference images. For instance, FS6D [17] designed a dense prototype matching framework by extracting and matching dense RGBD prototypes with transformers. After the correspondence is established, Umeyama [61] algorithms are utilized for pose estimation. OnePose/Onepose++ [15, 57] apply the Structure from Motion (SfM) method to reconstruct a sparse point cloud of the unseen object using all reference viewpoints. They then employ an attention-based network to predict the correspondence between 2D pixels and the reconstructed point clouds to estimate the object pose. For the latter, Multi-view references

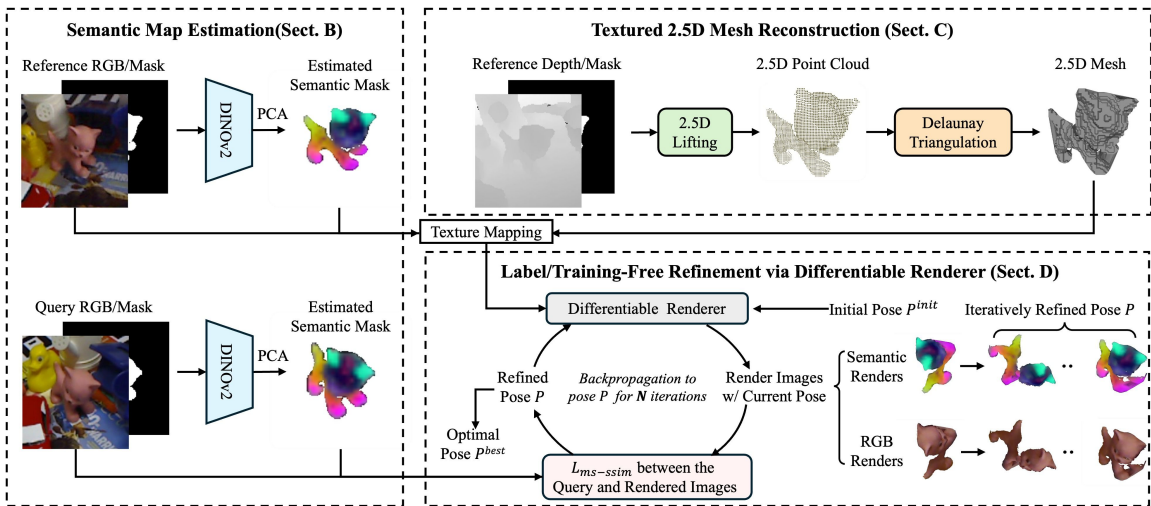


Fig. 2. **The overview of the proposed method.** Given an RGB-D reference and an RGB query, we extract the semantic maps from a pretrained DINOv2 model [44] for both reference and query. Then, the reference 2.5D front-surface mesh is reconstructed by the depth input without hallucination, which is subsequently texture-mapped by its RGB and semantic images. By leveraging a differentiable renderer [25], we generate the rendered RGB and semantic maps using the textured 2.5D reference mesh under a novel view/pose. Finally, the rendered RGB and semantic maps are compared to their query counterparts, producing losses and back-propagating the gradients through the differentiable renderer to refine the relative pose.

can be reviewed as templates for retrieval when plenty of views exist, or used to reconstruct the 3D object models for template rendering, similar to the CAD-based methods. As an illustration, Gen6D [38] selects the closest reference view for the query image, and then refines the pose through the 3D feature volume constructed from both the reference and query images. Notably, Gen6D requires more than 200 reference images for initial pose selection. On the contrary, LatentFusion [46] reconstructs a latent 3D representation of an object to present an end-to-end differentiable reconstruction and rendering pipeline, and then estimates the pose through gradients update. Since a 3D object representation can be reconstructed utilizing the multi-view information, FoundationPose [68] proposed a unified framework to support both CAD-based and multi-view supported setups. When no CAD model is available, they leverage multi-view references to build a neural implicit representation, which is then used for render-and-compare.

D. Generalizable Relative Pose Estimation

Recent methods [32, 75, 76, 77] highlight the importance of formulating object pose estimation as a relative pose estimation problem. Specifically, [77] and [76] address situations where only a single-view reference image is available. [77] evidence that some state-of-the-art feature matching approaches [53], [56], [14] fail to generate reliable correspondence between the reference-query pair, while energy-base methods [32, 75] struggles to capture 3D information. Instead, 3DAHV [77] introduces a framework of hypothesis and verification for generating and evaluating multiple pose hypotheses. Following 3DAHV, DVMNet [76] directly lifts the 2D image features to 3D voxel information in a hypothesis-free way, computing the relative pose estimation in an end-to-end fashion by aligning the 3D voxels.

III. METHOD

Following the render-and-compare paradigm, current generalizable pose estimation methods often rely on rotatable 3D

CAD models or well-calibrated multi-view images, imposing challenges to acquire the 3D CAD models or expensive pose calibration, especially for previously unseen objects. We instead focus on the generalizable **relative** pose estimation defined in [76, 77], which aims to estimate the relative pose between a reference-query pair, using only a single reference with an arbitrary pose as canonical (without calibration). Our method differs from [76, 77] in not requiring labeled relative pose to train an estimation network.

A. Overview

Taking an RGB query and an RGB-D reference as input, our method establishes a refinement optimization under the render-and-compare framework, by leveraging a 2.5D (i.e., RGB-D) shape of the reference, a pair of semantic maps for both the query and the reference acquired by a pretrained DINOv2 model [44] along with the corresponding RGB maps, and a differentiable renderer to backpropagate the gradients. Note that the 2.5D shape is exploited due to the inherent difficulty of accurately hallucinating the 3D shape of unseen objects when relying solely on a single RGB-D image. This challenge further complicates the task of relative pose estimation, as the hallucinated 3D shape must align precisely with the query to achieve a successful estimation.

Formally, by using *subscript* to denote query or reference, our method starts with an RGB pair I_r and I_q for both reference and query, as well as a depth map D_r for the reference. We proposed to estimate the relative pose between I_r and I_q , assisted by D_r . To this end, we first infer the semantic maps S_r and S_q from I_r and I_q exploiting a pretrained DINOv2 model [44]. Then, we construct a 2.5D mesh model M_r for the reference object based on D_r , to formulate an RGB and semantic maps textured 2.5D mesh $\mathcal{M}_r = \{M_r, I_r, S_r\}$. Subsequently, the textured 2.5D reference mesh \mathcal{M}_r is rotated with an (arbitrary) initial pose P by a differentiable renderer [25] to generate novel $I_r(P)$ and $S_r(P)$. Finally, the generated $I_r(P)$ and $S_r(P)$ are compared with the query I_q

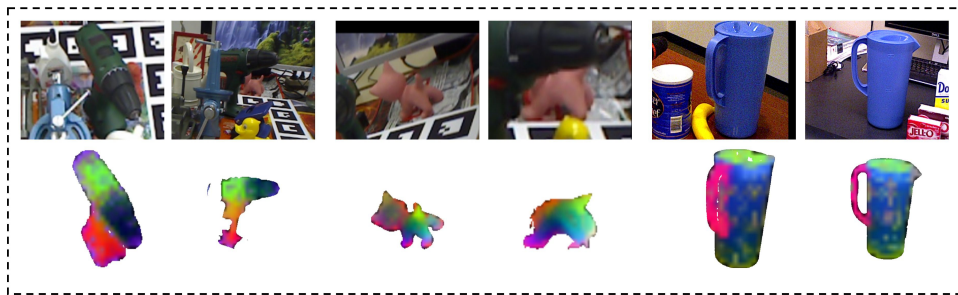


Fig. 3. **Illustration of the semantic maps estimated by DINOv2 [44], demonstrating promising zero-shot performance even for texture-less objects.**

and S_q , producing a refinement loss and consequently back-propagate gradients to P through the differentiable renderer. Our method operates the render-and-compare procedure in a self-supervised and network-free manner, without labeling or training.

The overview of the proposed method is illustrated in Fig. 2. We detail the comprising elements of our method in the following sections, i.e., **semantic map estimation** in Sect. III-B, **textured 2.5D mesh reconstruction** in Sect. III-C, and **label/training-free refinement via differentiable renderer** in Sect. III-D.

B. Semantic Map Estimation

In order to estimate the relative pose, human intelligence may unconsciously infer the semantics of the reference-query pair. Subsequently, coarse correspondence can be established with those semantics, resulting in three-fold benefits: it (i) helps to filter out the large non-overlapped part under a substantial pose difference, (ii) alleviates the influence of occlusions, and (iii) eases the degraded optimization of the relative pose estimation.

Benefit from the rapid development of large pretrained models, an elegant off-the-shelf semantic feature extractor is available as DINO/DINOv2 [6, 44], which shows great zero-shot generalize-ability to diverse (even texture-less) objects (see Fig. 3 for some examples). We thus incorporate the off-the-shelf DINOv2 model [44] to acquire the rich semantics of the input unseen objects.

Specifically, we utilize DINOv2 [44] as the semantic feature extractor $\Phi(\mathbf{x})$, which takes an RGB image I to produce a set of semantic features $F \in \mathbb{R}^{w \times h \times d}$. In order to texture F to the 2.5D model and facilitate the novel pose rendering, we use the principal component analysis (PCA) to reduce the dimension of F from d to 3, obtaining a semantic map S :

$$S = \text{PCA}(\Phi(I)), \quad \text{PCA} : \mathbb{R}^{w \times h \times d} \rightarrow \mathbb{R}^{w \times h \times 3}. \quad (1)$$

By feeding Eq. (1) with I_q and I_r , we can obtain the semantic maps for the query and the reference, S_q and S_r , respectively.

C. Textured 2.5D Mesh Reconstruction

In this section, we reconstruct a rotatable 2.5D model of the reference given its depth map D_r , which is subsequently

used to generate novel renderings through the differentiable renderer. Note that our design avoids the challenging 3D hallucination of an unseen object from the depth map, as the hallucinated 3D shape must consistently align with the query for relative pose estimation.

Specifically, given the depth map D_r of the reference, we lift the coordinates of the image plane into the 3D space and obtain the 2.5D point clouds $X_r \in \mathbb{R}^{N \times 3}$ of the front surface. We then reconstruct the corresponding 2.5D mesh M_r from X_r , to facilitate the rasterization in the renderer. Since the xy coordinates of X_r are sampled regularly from the 2D grids, reconstructing M_r from X_r can be easily achieved by the Delaunay triangulations [26]. Finally, we texture M_r with both color and semantic maps, obtaining $\mathcal{M}_r = \text{TextMap}(M_r, I_r, S_r)$ for rendering under novel poses.

Note that as discussed in Sect. I-A (Applicability), our method possesses the potential of using only an RGB reference and estimating an imprecise depth map exploiting an off-the-shelf generalizable depth estimator. Good estimation is validated in supplementary material given an imprecise and noising depth. We leave training a generalizable depth estimator as our future work to avoid possible distractions in this paper.

D. Label/Training-Free Refinement via Differentiable Renderer

Our last module of label/training-free refinement is constructed by a differentiable renderer, which takes the textured 2.5D reference mesh \mathcal{M}_r and a pose P as input, then renders a novel RGB image and a novel semantic map under the view P . By implementing the pose P as a random variable, the render-and-compare/reprojection loss can be back-propagated directly to P , ensuring the label/training-free and zero-shot unseen generalization merits of our proposed method.

Formally, by assuming a perspective camera, we leverage a recent differentiable renderer `nvidiffrast` [25], denoted as \mathcal{R} , to generate novel RGB and semantic maps, $I_r(P)$ and $S_r(P)$, from the textured 2.5D reference mesh \mathcal{M}_r , an arbitrary pose P , and the camera intrinsics K :

$$I_r(P), S_r(P) = \mathcal{R}(P, \mathcal{M}_r, K) \quad (2)$$

Back Surface Culling. As the reconstructed mesh is only 2.5D representing the front surface, it is crucial to conduct the back-surface culling during the rendering to filter out the

incorrect back-facing polygons. Specifically, for every triangle of the mesh, we first calculate the dot product of their surface normal and the camera-to-triangle (usually set to $[0, 0, 1]$) and then discard all triangles whose dot product is greater or equal to 0 [74]. Please also see the ablation with and without the back-surface culling in Table V.

Finally, the pose P can be optimized to align the rendered $I_r(P)$ and $S_r(P)$ with the query I_q and S_q , with the re-projection loss calculated by:

$$L(P) = L_1 \{I_r(P); I_q\} + L_2 \{S_r(P); S_q\}, \quad (3)$$

where $L(P)$ is the final loss to optimize the pose P , and we implement both losses by the multi-scale structural similarity (MS-SSIM) [78] as the following:

$$L_1 = 1 - \text{ms-ssim} \{I_r(P); I_q\}, \quad (4)$$

$$L_2 = 1 - \text{ms-ssim} \{S_r(P); S_q\}, \quad (5)$$

Equation (3) enables us to optimize P simply by gradient descent.

Initialization. As revealed in the majority of prior arts [24, 29, 42, 46], a good initialization significantly boosts the performance of the render-and-compare framework. To this end, we implement our initialization by evenly sampling candidate poses on a sphere and chasing the best one. Specifically, we first sample m viewpoints (azimuth and elevation angles) uniformly using a Fibonacci lattice [13], then uniformly sample n in-plane rotation angles for each viewpoint, producing $t = m * n$ poses as the initializing candidates. By rendering both RGB and semantic maps of those candidate poses, we are able to calculate the re-projection loss by Eq. (3) (without back-propagation in this phase) and choose the pose with the minimal loss as our initialization P^{init} .

Given the initialized pose P^{init} , we perform N iterations with gradient back-propagation to carry out the label/training-free refinement via the differentiable renderer. Our algorithm is detailed in Algorithm 1.

IV. EXPERIMENTS

In this section, we extensively validate our method on benchmark datasets including the LineMOD [18], YCB-V [69], and LineMOD-Occlusion (LM-O) [3] datasets. We detail the experimental setup in the following.

A. Experimental Setups

State-of-the-art Methods for Comparison. As shown in Table I, there does not exist a method applying the challenging setting of label/training-free and a single reference-query pair like ours. Therefore we choose the state-of-the-art methods that share the closest experimental setups, which are **ZSP** [14], **LoFTR** [56], **RelPose++** [32], **3DAHV** [77], and **DVMNet** [76]. Specifically, for **ZSP**, though it was originally proposed to process multiple queries, it is able to accept one RGB-D query as input. We report its performance based on the single RGB-D query and single RGB-D reference pair. For **LoFTR**, we use its pretrained weights released by the authors [56]. The weights of **DVMNet**, **3DAHV**, and **RelPose++** are

Algorithm 1 Generalizable Label/Training-Free Refinement

Input: Reference RGB and depth I_r, D_r ; query RGB I_q ; differentiable renderer \mathcal{R} ; pretrained DINOv2 model Φ , iteration quota N , learning rate α , camera intrinsic K .

- 1: $S_q \leftarrow \text{PCA}(\Phi(I_q)), S_r \leftarrow \text{PCA}(\Phi(I_r))$
- 2: $M_r \leftarrow \text{DelaunayTriangulations}(I_r, D_r)$
- 3: $\mathcal{M}_r \leftarrow \text{TextMap}(M_r, I_r, S_r)$

▷ **Sampling Poses for Initialization**

- 4: $\{P^1, P^2, \dots, P^n\} \leftarrow \text{Uniformly_sampling}()$
- 5: $\mathbf{P} = \{P^1, P^2, \dots, P^n\}$
- 6: $I_r(\mathbf{P}), S_r(\mathbf{P}) \leftarrow \mathcal{R}(\mathbf{P}, \mathcal{M}_r, K)$
- 7: $P^{\text{init}} = \arg \min_{P^i \in \mathbf{P}} L_1 \{I_r(P^i); I_q\} + L_2 \{S_r(P^i); S_q\}$

▷ **Label/Training-Free Refinement via Diff. Renderer**

- 8: $P \leftarrow P^{\text{init}}$
- 9: **for** $i < N$ **do**
- 10: $I_r(P), S_r(P) \leftarrow \mathcal{R}(P, \mathcal{M}_r, K)$
- 11: $L(P) = L_1 \{I_r(P); I_q\} + L_2 \{S_r(P); S_q\}$
- 12: $P \leftarrow \text{GradientDescent}(L(P), \alpha)$
- 13: **end for**

Output: P

retrained on-demand to achieve their best performance (for the details, see the following *Benchmark Experiments*, and the table captions of Table II, Table III and Table IV).

Datasets. The experiments are carried out on three benchmark object pose estimation datasets, i.e., LineMOD dataset [18] comprises 13 real objects, each depicting a single low-textured object on varying lighting conditions with approximately 1,200 images. LineMOD-Occlusion (LM-O) [3] consists of 1,214 images of the 8 occluded objects, extracted from the LineMOD dataset, the average visible fraction of objects in LM-O is 79.45%. YCB-V [69] encompasses over 110,000 real images featuring 21 objects characterized by severe occlusion and clutter, it exhibits an average visible object fraction of 87.15%.

Evaluation Metric. Following [76] and [77], we report mean angular error across sampled reference-query pairs. We also evaluate on important metrics of $\text{Acc}@5/10/15/30^\circ$, i.e., the percentage of the predictions that are within $5/10/15/30^\circ$, which can be more rigorous (e.g., $\text{Acc}@5^\circ$) and better characterize the performance. The degree of the pose difference between the ground truth R_{gt} and the predictions \hat{R} is calculated by the geodesic distance D :

$$D = \arccos \left((\text{tr}(\Delta R_{gt}^T \Delta \hat{R}) - 1) / 2 \right) / \pi \quad (6)$$

Benchmark Experiments. The in-dataset networks of the state-of-the-art DVMNet, 3DAHV, and RelPose++ methods need to be trained on the leave-out subset which comes from the same dataset as the testing subset but does not include the testing objects. For a fair comparison, on the LineMOD dataset, we follow the experiments in DVMNet [76] and 3DAHV [77] to evaluate 5 objects (i.e., benchvise, camera, cat, drill, duck). For the YCB-V experiments, we design a similar training protocol to enable the comparison with DVMNet, 3DAHV, and RelPose++, where we randomly sample 8 objects (i.e., tuna_fish_can, pudding_box, banana, pitcher_base, mug, power_drill, large_clamp, foam_brick) for

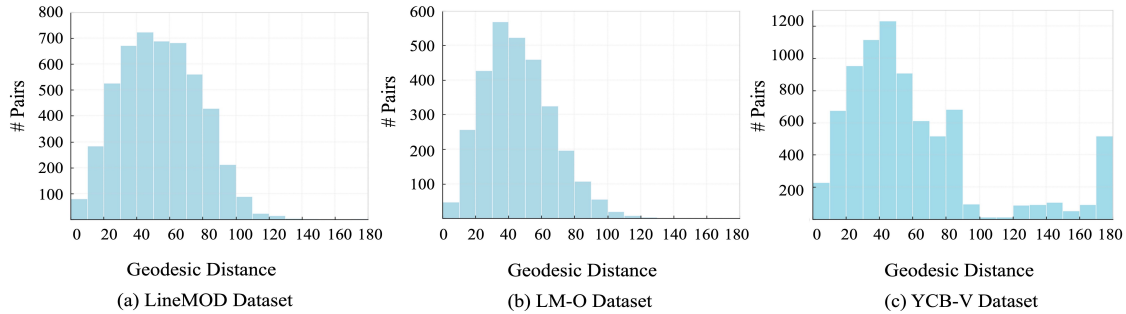


Fig. 4. Histograms of the geodesic distance between the sampled reference-query pairs. The in-plane rotation is included in calculating the histograms.

evaluation, leaving the remaining 13 objects to train these three methods. Following DVMNet [76], we evaluate 3 unseen objects on the LM-O dataset (i.e., cat, driller, and duck). Since the challenging LM-O dataset is typically used solely for evaluation, we directly use the same weights for DVMNet and 3DAHV that were trained in the LineMOD experiments.

Since the results on the rigorous metrics of $\text{Acc}@5/10^\circ$ are not reported in the 3DAHV [77] and DVMNet [76] paper, we thus retrain them using the code released by the authors for the $\text{Acc}@5/10^\circ$ evaluation.

Moreover, as a label/training-free method, the performance of our method can be assessed on all the objects of LineMOD, YCB-V, and LM-O datasets, without the need to leave out any training data or leverage any external dataset. We report the performance of our method on the complete LineMOD, YCB-V, and LM-O datasets in Tables S3, S4, and S5 of the supplementary material.

In-dataset and Cross-dataset Evaluation. Beyond the unseen objects generalization, we also test the dataset-level generalization for the state-of-the-art network-based methods DVMNet and 3DAHV, reporting both the *in-dataset* and *cross-dataset* performance. In short, *in-dataset* and *cross-dataset* differ in whether the network needs to be finetuned on a subset that comes from the same dataset with the testing set (though not including the testing objects). Therefore, a good *cross-dataset* performance demonstrates better generalization in terms of the dataset, as the network only needs to be trained once on a large-scale external dataset without finetuning. Specifically, for the *in-dataset* experiments, we follow the exact training protocols of DVMNet [76] and 3DAHV [77], which first pretrain on an external large-scale dataset Objaverse [11] then finetune on a certain dataset (e.g., LineMOD or YCB-V). For *cross-dataset* experiments, we use the pretrained weights from Objaverse directly without finetuning.

Note that the evaluation of our method, ZSP, and LoFTR does not involve a finetuning phase, demonstrating that our method, ZSP, and LoFTR naturally generalize to an arbitrary dataset⁴.

Reference-Query Pair Generation. We follow DVMNet [76] and 3DAHV [77] to generate the reference-query pairs with sufficient overlaps for training and testing. Specifically, given a reference rotation R_r and a query rotation R_q , we first convert the rotation matrices R_r and R_q to Euler angles

$(\alpha_r, \beta_r, \gamma_r)$ and $(\alpha_q, \beta_q, \gamma_q)$. Since the in-plane rotation γ does not influence the overlaps between the reference and query pair, it is set to 0 and converted back to the rotation matrix, i.e., $\tilde{R} = h(\alpha, \beta, 0)$ with h being Euler-angle to rotation matrix transformation. The overlap between the query and the reference is measured by the geodesic distance (i.e., the pose difference in degree) between their in-plane-omitted rotation matrices \tilde{R}_q and \tilde{R}_r using Eq. (6). Finally, following DVMNet [76] and 3DAHV [77], we select the sampled pairs with \tilde{D} less than 90° .

Following DVMNet [76] and 3DAHV [77], for each object, we generate 1000 pairs for testing, and 20000 pairs for training DVMNet, 3DAHV, and RelPose++. Figure 4 illustrates the histograms depicting the statistics of the pairwise pose difference (geodesic distance between rotation matrices R_r and R_q) on the three datasets. All the experiments are carried out on the same testing reference-query pairs.

Implementation Details. For semantic feature extraction, we employ the output tokens from the last layer of the DINOv2 ViT-L model [44]. We use nvdiffrast [25] as our differentiable renderer. We uniformly sample $m = 200$ viewpoints and $n = 20$ in-plane rotations (resulting in 4000 initialization candidates), the maximal iteration number for differentiable rendering is set to $N = 30$. To backpropagate the refinement losses, we use an Adam optimizer [22] of 0.01 initial learning rate and decay by a ReduceLROnPlateau scheduler. All the experiments are conducted on a single NVIDIA 4090 GPU.

B. Experimental Results on the LineMOD Dataset

The results on the LineMOD dataset are illustrated in Table II. We paste the performances of RelPose++ from the 3DAHV paper [77]. We leave the $\text{Acc}@5/10^\circ$ performance of RelPose++ blank as those were not reported in [77] and the (pre-) training code of RelPose++ on the external large-scale Objaverse dataset is not available.

Table II shows that our *label and training-free* method significantly outperforms the *supervised* state-of-the-art DVMNet w.r.t. all the metrics. In addition, the state-of-the-art methods DVMNet and 3DAHV face challenges in generalizing across different datasets, i.e., their in-dataset results substantially outperform their cross-dataset counterparts. In contrast, our approach, without training a network, inherently generalizes across diverse datasets directly. Especially, our method significantly outperforms DVMNet (in-dataset) for 21.6% and 32.08% w.r.t. the rigorous $\text{Acc}@5/10^\circ$. The qualitative results

⁴This is achieved by that 1) the pose estimation phase of our method, ZSP, and LoFTR are general and do not involve learning a network, and 2) they all use generalizable feature extractors, i.e., DINOv2 or LoFTR.

TABLE II

EXPERIMENTAL RESULTS ON LINEMOD. WE ILLUSTRATE BOTH THE EXPERIMENTAL SETTINGS AND THE PERFORMANCE. IN THE RGB-D CATEGORY, BOTH MEANS REQUIRING RGB-D IMAGE FOR BOTH QUERY AND REFERENCE. $\text{Acc}@t^\circ$ MEASURES THE PERCENTAGE OF THE ESTIMATED POSE WITHIN t° W.R.T. THE GROUND-TRUTH.

Method	Settings			Error↓ Mean Err	Acc @ t° (%) ↑			
	Training	Label	RGB-D		30°	15°	10°	5°
ZSP	✗	label-free	both	102.33	8.20	2.22	0.90	0.18
LoFTR	✓	pose+depth	no	63.88	23.94	10.80	6.82	2.42
RelPose++	✓	pose	no	46.60	42.50	15.80	–	–
3DAHV (cross-dataset)	✓	pose	no	69.24	21.20	5.52	2.52	0.44
3DAHV (in-dataset)	✓	pose	no	42.77	59.16	25.92	11.36	2.16
DVMNet (cross-dataset)	✓	pose	no	47.47	36.44	13.14	5.92	1.08
DVMNet (in-dataset)	✓	pose	no	33.28	55.02	22.38	10.66	2.72
Ours (init. only)	✗	label-free	reference	<u>32.24</u>	<u>70.88</u>	<u>48.28</u>	<u>29.76</u>	<u>6.66</u>
Ours (init. + refine)	✗	label-free	reference	29.93	72.06	54.90	42.74	24.32

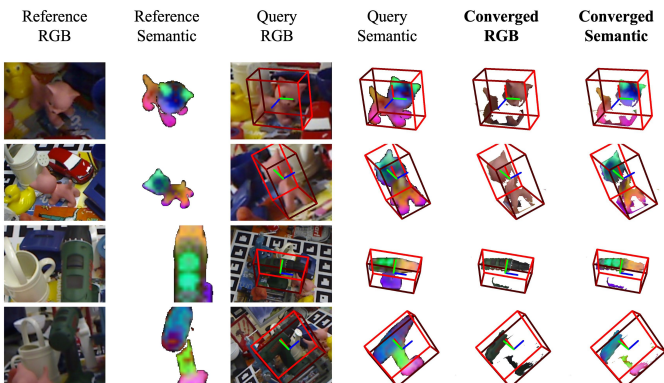


Fig. 5. **Qualitative results on LineMOD.** This figure shows that our method can handle partially occluded and texture-less objects. We use a 3D bbox to denote poses.

of our method are shown in Fig. 5, and comparisons with different methods are presented in Fig. S3 of the supplementary material. Our results on all the LineMOD objects are detailed in Table S3 of the supplementary material.

C. Experimental Results on the YCB-V Dataset

To compare with the state-of-the-art DVMNet [76], 3DAHV [77] and RelPose++ [32], we follow the protocols discussed in Sect. IV-A (In-dataset and Cross-dataset Evaluation) to obtain the in-dataset and cross-dataset performance of DVMNet [76] and 3DAHV [77], while RelPose++ is trained on the YCB-V dataset only. The performance on the YCB-V dataset is reported in Table III, where our method exhibits a significant improvement of 11.02% and 17.83% w.r.t. the state-of-the-art DVMNet (in-dataset), respectively on the challenging $\text{Acc}@5/10^\circ$ metrics. We showcase the qualitative results of our method on the YCB-V dataset in Fig. 6, and those across different methods can be found in Fig. S2 of the supplementary material. Our results on all the YCB-V objects are shown in Table S5 of the supplementary material.

D. Experimental Results on the LM-O Dataset

Finally, we carry out the experiments on the challenging LM-O Dataset with severe occlusions. Following DVMNet [76], we conduct the experiments on three unseen objects of the LM-O dataset, i.e., cat, driller, and duck. We note that the LM-O dataset is typically used solely for evaluation. Therefore, the results of DVMNet and 3DAHV are evaluated

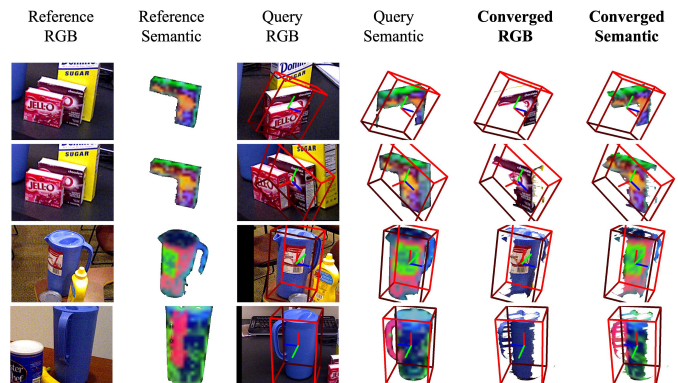


Fig. 6. **Qualitative results on YCB-V.** This figure shows that our method can handle partially occluded and texture-less objects. We use a 3D bbox to denote poses.

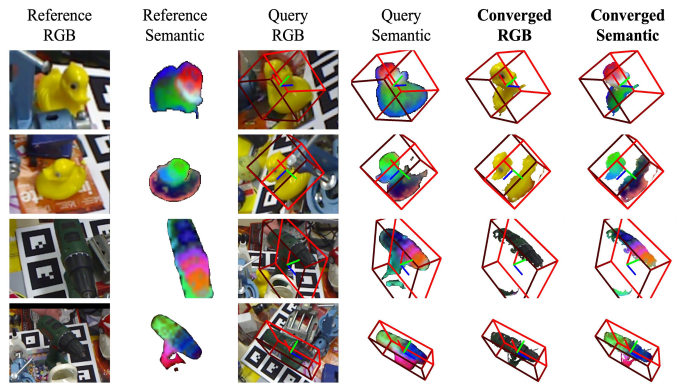


Fig. 7. **Qualitative results on LM-O.** This figure shows that our method can handle severely occluded and texture-less objects. We use a 3D bbox to denote poses.

utilizing the weights finetuned on LineMOD. Nevertheless, since the weights of RelPose++ for the LineMOD dataset have not been released yet and LM-O (with only 8 objects) cannot provide sufficient leave-out data to train RelPose++, we thus do not include RelPose++ for comparison. The results from Table IV demonstrate the promising performance of our method on the severely occluded LM-O dataset. We showcase our performance on the LM-O dataset in Fig. 7, and those across different methods are illustrated in Fig. S2 of the supplementary material. Our results on all the LM-O objects can be found in Table S4 of the supplementary material.

We observe that our results in terms of *Mean Err* are inferior to the in-dataset results of the state-of-the-art DVMNet and

TABLE III

EXPERIMENTAL RESULTS ON YCB-V. THE PERFORMANCE OF DVMNET, 3DAHV, AND RELPOSE++ IS OBTAINED BY TRAINING ON A LEAVE-OUT SUBSET OF 13 OBJECTS. OTHER PARAMETERS/SYMBOLS ARE THE SAME AS THOSE IN TABLE II.

Method	Settings			Error↓ Mean Err	Acc @ t° (%) ↑			
	Training	Label	RGB-D		30°	15°	10°	5°
ZSP	✗	label-free	both	88.65	15.63	5.82	2.89	0.65
LoFTR	✓	pose+depth	no	68.65	29.45	13.56	7.9	3.19
RelPose++	✓	pose	no	57.41	23.60	7.13	3.28	0.76
3DAHV (cross-dataset)	✓	pose	no	66.61	35.06	16.18	8.28	1.50
3DAHV (in-dataset)	✓	pose	no	69.48	44.54	28.41	16.29	3.59
DVMNet (cross-dataset)	✓	pose	no	54.12	41.28	17.11	9.35	2.53
DVMNet (in-dataset)	✓	pose	no	48.88	51.71	27.04	14.03	3.16
Ours (init. only)	✗	label-free	reference	48.65	56.59	35.68	21.86	5.36
Ours (init. + refine)	✗	label-free	reference	47.09	56.63	42.69	31.86	14.18

TABLE IV

EXPERIMENTAL RESULTS ON LM-O. LM-O IS TYPICALLY USED SOLELY FOR TESTING WITH ONLY 8 OBJECTS UNDER SEVERE OCCLUSIONS. THE RESULTS OF DVMNET AND 3DAHV ARE TESTED DIRECTLY USING THE WEIGHTS TRAINED ON LINEMOD. SINCE THE MODEL WEIGHTS OF RELPOSE++ USED IN TABLE II WERE NOT RELEASED, WE DO NOT COMPARE OUR METHOD WITH RELPOSE++ IN THIS EXPERIMENT. OTHER PARAMETERS/SYMBOLS ARE THE SAME AS THOSE IN TABLE II.

Method	Settings			Error↓ Mean Err	Acc @ t° (%) ↑			
	Training	Label	RGB-D		30°	15°	10°	5°
ZSP	✗	label-free	both	103.70	7.10	1.67	0.60	0.07
LoFTR	✓	pose+depth	no	68.15	20.63	9.00	4.87	1.87
3DAHV (cross-dataset)	✓	pose	no	55.05	32.83	9.47	4.40	0.53
3DAHV (in-dataset)	✓	pose	no	62.30	40.29	10.57	3.84	0.57
DVMNet (cross-dataset)	✓	pose	no	<u>51.75</u>	35.52	12.94	5.30	1.33
DVMNet (in-dataset)	✓	pose	no	48.55	38.62	14.14	7.37	1.87
Ours (init. only)	✗	label-free	reference	55.94	<u>53.80</u>	<u>31.72</u>	<u>17.18</u>	<u>2.80</u>
Ours (init. + refine)	✗	label-free	reference	55.09	54.50	34.97	23.00	6.83

3DAHV (though our method exhibits better Acc@ t° results). This can be attributed to the extensive occlusions presented in the LM-O dataset, which lead to numerous testing pairs lacking adequate overlap. Consequently, those testing pairs are difficult to handle by all the methods (and also challenging for humans). We show those samples as failure cases in Fig. 8 of Sect. V-E, as well as investigating the angle error distribution (ranging from 0 to 180 degrees) on the LM-O dataset in Fig. S1 of the supplementary materials. The statistics reveal that at lower angle error thresholds (e.g., for $t \leq 10, 20$ in Acc@ t°), our approach substantially outperforms both DVMNet and 3DAHV. This indicates that for test pairs with sufficient overlaps (i.e., match-able testing pairs), our method delivers superior performance compared to the state-of-the-art DVMNet and 3DAHV.

V. ABLATION ANALYSIS

We carefully investigate the following issues by ablation: 1) the contribution of each comprising element of our method, including *the back-surface culling*, and the usage of *RGB* or *semantic* modality in Sect. V-A; 2) the effects of different initialization strategies in Sect. V-B; 3) the effects of different refinement iterations in Sect. V-C; 4) the inference time statistics of our method in Sect. V-D; and 5) the failure cases illustrations from the LM-O dataset in Sect. V-E.

A. The Contributions of the Proposed Comprising Elements

Despite the simplicity of our method, we are interested in investigating the influences for each of our comprising elements, namely *the back-surface culling*, and the usage of

RGB or *semantic* modality. We perform those ablations on the LineMOD, and the results are reported in Table V.

As expected, removing each of our comprising elements results in a decreased performance, because all of them are exploited with clear motivations. Nonetheless, the encouraging observation is that our method is able to deliver promising results using only the **RGB** modality without the **semantic** map. This further extends the applicability of our method when the pretrained DINOv2 model is not available or when the DINOv2 model cannot produce reasonable outputs (though the latter case could be rare).

TABLE V

THE CONTRIBUTIONS OF THE PROPOSED COMPRISING ELEMENTS ON THE LINEMOD DATASET.

Metrics	Mean Err↓	Acc @30°↑	Acc @15°↑	Acc @10°↑	Acc @5°↑
w/o culling	38.09	67.46	52.32	40.82	23.58
only RGB	36.26	67.42	50.40	37.70	19.62
only semantic	31.31	69.32	50.86	38.80	19.22
Ours	29.93	72.06	54.90	42.74	24.32

B. Effects of Different Initialization Strategies

The pose estimation performance under the render-and-compare paradigm is largely affected by the initialization [24, 29, 37, 42, 46, 70]. In the following, we investigate different initializations including: 1) *random initialization*, where we randomly sample candidate poses and choose the best one; and 2) *uniform initialization*, where the candidate poses are uniformly sampled from a Fibonacci lattice with in-plane rotations [13], as detailed in Sect. III-D (Initialization). For the latter, we also examine different densities of the sampling, i.e., the Fibonacci lattice viewpoints including 100 and 200, and in-plane rotations including 20 and 50.

TABLE VI
EFFECTS OF DIFFERENT INITIALIZATION STRATEGIES USING THE LINEMOD DATASET. WE EVALUATE DIFFERENT INITIALIZATION STRATEGIES (ROWS 1-2) AS WELL AS THE SAMPLING DENSITY (ROWS 3-5).

Initial Strategy	Sampling Numbers	Error↓	Acc @ t° (%) ↑			
		Mean Err	30°	15°	10°	5°
Random Init.	4000	31.73	70.90	52.66	40.88	23.08
Uniform Init. (used in our experiments)	4000 (200 viewpoints, 20 in-plane rotations)	29.93	72.06	54.90	42.74	24.32
Uniform Init.	2000 (100 viewpoints, 20 in-plane rotations)	32.51	69.36	49.26	38.80	21.70
Uniform Init. (used in our experiments)	4000 (200 viewpoints, 20 in-plane rotations)	29.93	72.06	54.90	42.74	24.32
Uniform Init.	10000 (200 viewpoints, 50 in-plane rotations)	29.13	73.30	57.46	44.92	25.02

Table VI illustrates the performance of different initialization strategies using the LineMOD dataset, which demonstrates that 1) the *uniform initialization* outperforms the *random initialization*, and 2) uniform initialization with *denser sampling* leads to better performance. In our experiments, we choose *uniform initialization with 4000 samples* (200 Fibonacci lattice viewpoints times 20 in-plane rotations) to balance the performance and the efficiency.

C. Effects of Different Refinement Iterations.

Table VII illustrates the impact of the iteration numbers for our label/training-free refinement using the LineMOD dataset. It shows that the improvement becomes marginal after the iteration number N exceeds 30. We thus set the iteration number to $N = 30$ to achieve a balance between performance and efficiency.

TABLE VII
EFFECTS OF DIFFERENT REFINEMENT ITERATIONS ON LINEMOD.

Iterations N	Mean Err↓	Acc @30°↑	Acc @15°↑	Acc @10°↑	Acc @5°↑
10	30.46	71.92	53.40	39.98	19.86
20	30.16	72.04	54.18	41.84	22.60
30 (used in our exp.)	29.93	72.06	54.90	42.74	24.32
50	29.86	72.10	54.94	42.92	25.18
100	29.73	72.12	55.26	43.60	25.64

D. The Statistics of Our Inference Time

We collect the inference time per reference-query pair, averaged across the LineMOD datasets on a single 4090 GPU. We report the runtime for each stage of our method in Table VIII. Note that the initialization is efficient with much more candidate samples than the refinement, because those initializing candidate samples can be evaluated in parallel without backpropagation. Table VIII demonstrates the efficiency of our method with a per-pair runtime of 4.85 seconds in total.

TABLE VIII
INFERENCE TIME STATISTICS OF OUR METHOD ON LINEMOD.

Semantic Fea. Extraction	Pose Initialization	Refinement	Total
0.24 s	3.46 s	1.03 s	4.85 s

E. Illustrations of the Failure Cases

We show our failure cases on the LM-O dataset in Fig. 8, where there do not exist sufficient overlaps between the query and the reference. We note such an extremely degraded case as our limitation and discuss it in Sect. VI (Limitations and Future Works).

VI. DISCUSSIONS AND CONCLUSIONS

Limitations and Future Works. Our method has the following two limitations. Firstly, our method necessitates the depth information of the reference object as an input. Although

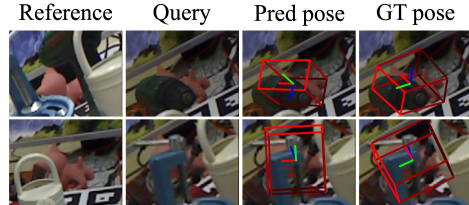


Fig. 8. **Failure Cases of our method on the LM-O dataset**, where there do not exist sufficient overlaps between the query and the reference due to severe occlusions.

this is a one-time requirement per object, the need for depth data can restrict the applicability of our method where a depth sensor is absent. To acquire the depth of the reference image, we evaluated several advanced monocular depth estimation algorithms, including [2, 50, 51, 72]. However, we found that these methods often struggle to generalize across different object types. Despite this, our empirical results, presented in Table S1 of the supplementary materials, demonstrate that our method remains robust with imprecise depth (simulated by adding noise to the ground-truth depth). This suggests that the current limitations are likely to be overcome once an object-generalizable depth estimator becomes available.

Secondly, our method is likely to fail in the severely degraded scenario where there do not exist adequate overlaps between the query and the reference (possibly caused by occlusions, e.g., Fig. 8). Future research with simultaneous render-and-compare and object completion (with minimal inconsistent hallucination) is a promising direction to explore.

We also note an additional future direction about adaptively determining the loss weights of the RGB pair and the semantic pair in Eq. (3) (preferably adapting in each refinement step), though we empirically showed that simply using equal weights (i.e., both set to 1) leads to promising results.

Conclusions. In this paper, we addressed the challenging generalizable relative pose estimation under a rigorous circumstance with only a single RGB-D reference and single RGB query pair as input, and the pose label is not a priori. We establish our label- and training-free method following the render-and-compare paradigm, by exploiting 1) the 2.5D (i.e., RGB-D) rotatable reference mesh, 2) the semantic maps of both query and reference (extracted by a pretrained large vision model DINOv2), and 3) a differentiable renderer to produce and back-propagate losses to refine the relative pose. We carried out extensive experiments on the LineMOD, LM-O, and YCB-V datasets. The results demonstrate that our label/training-free approach surpasses the performance of state-of-the-art supervised methods, particularly excelling under the rigorous $\text{Acc}@5/10/15^\circ$ metrics.

REFERENCES

- [1] Pedram Azad, Tamim Asfour, and Ruediger Dillmann. Stereo-based 6d object localization for grasping with humanoid robot systems. In *2007 IEEE/RSJ International Conference on Intelligent Robots and Systems*, pages 919–924. IEEE, 2007. 1
- [2] Shariq Farooq Bhat, Reiner Birkel, Diana Wofk, Peter Wonka, and Matthias Müller. Zoedepth: Zero-shot transfer by combining relative and metric depth. *arXiv preprint arXiv:2302.12288*, 2023. 10
- [3] Eric Brachmann, Alexander Krull, Frank Michel, Stefan Gumhold, Jamie Shotton, and Carsten Rother. Learning 6d object pose estimation using 3d object coordinates. In *European conference on computer vision*, pages 536–551. Springer, 2014. 2, 6
- [4] Yannick Bukschat and Marcus Vetter. Efficientpose: An efficient, accurate and scalable end-to-end 6d multi object pose estimation approach. *arXiv preprint arXiv:2011.04307*, 2020. 3
- [5] Andrea Caraffa, Davide Boscaini, Amir Hamza, and Fabio Poiesi. Object 6d pose estimation meets zero-shot learning. *arXiv preprint arXiv:2312.00947*, 2023. 3
- [6] Mathilde Caron, Hugo Touvron, Ishan Misra, Hervé Jégou, Julien Mairal, Piotr Bojanowski, and Armand Joulin. Emerging properties in self-supervised vision transformers. In *Proceedings of the IEEE/CVF International Conference on Computer Vision*, pages 9650–9660, 2021. 5
- [7] Dengsheng Chen, Jun Li, Zheng Wang, and Kai Xu. Learning canonical shape space for category-level 6d object pose and size estimation. In *Proceedings of the IEEE/CVF Conference on Computer Vision and Pattern Recognition*, pages 11973–11982, 2020. 3
- [8] Jianqiu Chen, Mingshan Sun, Tianpeng Bao, Rui Zhao, Liwei Wu, and Zhenyu He. Zeropose: Cad-model-based zero-shot pose estimation. *arXiv preprint arXiv:2305.17934*, 2, 2023. 1, 2, 3
- [9] Kai Chen and Qi Dou. Sgpa: Structure-guided prior adaptation for category-level 6d object pose estimation. In *Proceedings of the IEEE/CVF International Conference on Computer Vision*, pages 2773–2782, 2021. 3
- [10] Wei Chen, Xi Jia, Hyung Jin Chang, Jinming Duan, Linlin Shen, and Ales Leonardis. Fs-net: Fast shape-based network for category-level 6d object pose estimation with decoupled rotation mechanism. In *Proceedings of the IEEE/CVF Conference on Computer Vision and Pattern Recognition*, pages 1581–1590, 2021. 3
- [11] Matt Deitke, Dustin Schwenk, Jordi Salvador, Luca Weihs, Oscar Michel, Eli VanderBilt, Ludwig Schmidt, Kiana Ehsani, Aniruddha Kembhavi, and Ali Farhadi. Objaverse: A universe of annotated 3d objects. In *Proceedings of the IEEE/CVF Conference on Computer Vision and Pattern Recognition*, pages 13142–13153, 2023. 2, 7
- [12] Yan Di, Fabian Manhardt, Gu Wang, Xiangyang Ji, Nassir Navab, and Federico Tombari. So-pose: Exploiting self-occlusion for direct 6d pose estimation. In *Proceedings of the IEEE/CVF International Conference on Computer Vision*, pages 12396–12405, 2021. 3
- [13] Álvaro González. Measurement of areas on a sphere using fibonacci and latitude–longitude lattices. *Mathematical Geosciences*, 42:49–64, 2010. 6, 9
- [14] Walter Goodwin, Sagar Vaze, Ioannis Havoutis, and Ingmar Posner. Zero-shot category-level object pose estimation. In *European Conference on Computer Vision*, pages 516–532. Springer, 2022. 2, 4, 6
- [15] Xingyi He, Jiaming Sun, Yuang Wang, Di Huang, Hujun Bao, and Xiaowei Zhou. Onepose++: Keypoint-free one-shot object pose estimation without cad models. *Advances in Neural Information Processing Systems*, 35:35103–35115, 2022. 1, 2, 3
- [16] Yisheng He, Wei Sun, Haibin Huang, Jianran Liu, Haoqiang Fan, and Jian Sun. Pvn3d: A deep point-wise 3d keypoints voting network for 6dof pose estimation. In *Proceedings of the IEEE/CVF Conference on Computer Vision and Pattern Recognition*, pages 11632–11641, 2020. 3
- [17] Yisheng He, Yao Wang, Haoqiang Fan, Jian Sun, and Qifeng Chen. Fs6d: Few-shot 6d pose estimation of novel objects. In *Proceedings of the IEEE/CVF Conference on Computer Vision and Pattern Recognition*, pages 6814–6824, 2022. 1, 2, 3
- [18] Stefan Hinterstoisser, Vincent Lepetit, Slobodan Ilic, Stefan Holzer, Gary Bradski, Kurt Konolige, and Nassir Navab. Model based training, detection and pose estimation of texture-less 3d objects in heavily cluttered scenes. In *Computer Vision—ACCV 2012: 11th Asian Conference on Computer Vision, Daejeon, Korea, November 5–9, 2012, Revised Selected Papers, Part I 11*, pages 548–562. Springer, 2013. 2, 6
- [19] Tomas Hodan, Daniel Barath, and Jiri Matas. Epos: Estimating 6d pose of objects with symmetries. In *Proceedings of the IEEE/CVF Conference on Computer Vision and Pattern Recognition*, pages 11703–11712, 2020. 3
- [20] Prakhar Kaushik, Aayush Mishra, Adam Kortylewski, and Alan Yuille. Source-free and image-only unsupervised domain adaptation for category level object pose estimation. *arXiv preprint arXiv:2401.10848*, 2024. 1
- [21] Wadim Kehl, Fabian Manhardt, Federico Tombari, Slobodan Ilic, and Nassir Navab. Ssd-6d: Making rgb-based 3d detection and 6d pose estimation great again. In *Proceedings of the IEEE international conference on computer vision*, pages 1521–1529, 2017. 3
- [22] Diederik P Kingma and Jimmy Ba. Adam: A method for stochastic optimization. *arXiv preprint arXiv:1412.6980*, 2014. 7
- [23] Alexander Kirillov, Eric Mintun, Nikhila Ravi, Hanzi Mao, Chloe Rolland, Laura Gustafson, Tete Xiao, Spencer Whitehead, Alexander C Berg, Wan-Yen Lo, et al. Segment anything. *arXiv preprint arXiv:2304.02643*, 2023. 3
- [24] Yann Labbé, Lucas Manuelli, Arsalan Mousavian, Stephen Tyree, Stan Birchfield, Jonathan Tremblay, Justin Carpentier, Mathieu Aubry, Dieter Fox, and Josef Sivic. Megapose: 6d pose estimation of novel objects via render & compare. *arXiv preprint arXiv:2212.06870*, 2022. 1, 2, 3, 6, 9
- [25] Samuli Laine, Janne Hellsten, Tero Karras, Yeongho Seol, Jaakko Lehtinen, and Timo Aila. Modular primitives for high-performance differentiable rendering. *ACM Transactions on Graphics (TOG)*, 39(6):1–14, 2020. 2, 4, 5, 7
- [26] Der-Tsai Lee and Bruce J Schachter. Two algorithms for constructing a delaunay triangulation. *International Journal of Computer & Information Sciences*, 9(3):219–242, 1980. 5
- [27] Taeyeop Lee, Byeong-Uk Lee, Myungchul Kim, and In So Kweon. Category-level metric scale object shape and pose estimation. *IEEE Robotics and Automation Letters*, 6(4):8575–8582, 2021. 3
- [28] Vincent Lepetit, Francesc Moreno-Noguer, and Pascal Fua. Eppn: An accurate o (n) solution to the pnp problem. *International journal of computer vision*, 81(2):155–166, 2009. 3
- [29] Yi Li, Gu Wang, Xiangyang Ji, Yu Xiang, and Dieter Fox. Deepim: Deep iterative matching for 6d pose estimation. In *Proceedings of the European Conference on Computer Vision (ECCV)*, pages 683–698, 2018. 3, 6, 9
- [30] Zhigang Li, Gu Wang, and Xiangyang Ji. Cdpn: Coordinates-based disentangled pose network for real-time rgb-based 6-dof object pose estimation. In *Proceedings of the IEEE/CVF International Conference on Computer Vision*, pages 7678–7687, 2019. 3
- [31] Ruyi Lian and Haibin Ling. Checkerpose: Progressive dense keypoint localization for object pose estimation with graph neural network. *arXiv preprint arXiv:2303.16874*, 2023. 3
- [32] Amy Lin, Jason Y Zhang, Deva Ramanan, and Shubham Tulsiani. Relpose++: Recovering 6d poses from sparse-view observations. *arXiv preprint arXiv:2305.04926*, 2023. 1, 2, 4, 6, 8
- [33] Jiehong Lin, Lihua Liu, Dekun Lu, and Kui Jia. Sam-6d: Segment anything model meets zero-shot 6d object pose estimation. *arXiv preprint arXiv:2311.15707*, 2023. 2, 3
- [34] Jiehong Lin, Zewei Wei, Changxing Ding, and Kui Jia. Category-level 6d object pose and size estimation using self-supervised deep prior deformation networks. In *European Conference on Computer Vision*, pages 19–34. Springer, 2022. 3
- [35] Jiehong Lin, Zewei Wei, Zhihao Li, Songcen Xu, Kui Jia, and Yuanqing Li. Dualposenet: Category-level 6d object pose and size estimation using dual pose network with refined learning of pose consistency. In *Proceedings of the IEEE/CVF International Conference on Computer Vision*, pages 3560–3569, 2021. 3
- [36] Jiehong Lin, Zewei Wei, Yabin Zhang, and Kui Jia. Vi-net: Boosting category-level 6d object pose estimation via learning decoupled rotations on the spherical representations. In *Proceedings of the IEEE/CVF International Conference on Computer Vision*, pages 14001–14011, 2023. 3
- [37] Lahav Lipson, Zachary Teed, Ankit Goyal, and Jia Deng. Coupled iterative refinement for 6d multi-object pose estimation. In *Proceedings of the IEEE/CVF Conference on Computer Vision and Pattern Recognition*, pages 6728–6737, 2022. 3, 9
- [38] Yuan Liu, Yilin Wen, Sida Peng, Cheng Lin, Xiaoxiao Long, Taku Komura, and Wenping Wang. Gen6d: Generalizable model-free 6-dof object pose estimation from rgb images. In *European Conference on Computer Vision*, pages 298–315. Springer, 2022. 1, 2, 3, 4
- [39] Fabian Manhardt, Gu Wang, Benjamin Busam, Manuel Nickel, Sven Meier, Luca Minciullo, Xiangyang Ji, and Nassir Navab. Cps++: Improving class-level 6d pose and shape estimation from monocular images with self-supervised learning. *arXiv preprint arXiv:2003.05848*, 2020. 3
- [40] Van Nguyen Nguyen, Thibault Groueix, Yinlin Hu, Mathieu Salzmann,

- and Vincent Lepetit. Nope: Novel object pose estimation from a single image. *arXiv preprint arXiv:2303.13612*, 2023. 1
- [41] Van Nguyen Nguyen, Thibault Groueix, Mathieu Salzmann, and Vincent Lepetit. Gigapose: Fast and robust novel object pose estimation via one correspondence. *arXiv preprint arXiv:2311.14155*, 2023. 2, 3
- [42] Van Nguyen Nguyen, Yinlin Hu, Yang Xiao, Mathieu Salzmann, and Vincent Lepetit. Templates for 3d object pose estimation revisited: Generalization to new objects and robustness to occlusions. In *Proceedings of the IEEE/CVF Conference on Computer Vision and Pattern Recognition*, pages 6771–6780, 2022. 1, 2, 3, 6, 9
- [43] Brian Okorn, Qiao Gu, Martial Hebert, and David Held. Zephyr: Zero-shot pose hypothesis rating. In *2021 IEEE International Conference on Robotics and Automation (ICRA)*, pages 14141–14148. IEEE, 2021. 1, 2, 3
- [44] Maxime Oquab, Timothée Darcet, Théo Moutakanni, Huy Vo, Marc Szafraniec, Vasil Khalidov, Pierre Fernandez, Daniel Haziza, Francisco Massa, Alaaeldin El-Nouby, et al. Dinov2: Learning robust visual features without supervision. *arXiv preprint arXiv:2304.07193*, 2023. 2, 4, 5, 7
- [45] Evin Pinar Örnek, Yann Labbé, Bugra Tekin, Lingni Ma, Cem Keskin, Christian Forster, and Tomas Hodan. Foundpose: Unseen object pose estimation with foundation features. *arXiv preprint arXiv:2311.18809*, 2023. 2, 3
- [46] Keunhong Park, Arsalan Mousavian, Yu Xiang, and Dieter Fox. Latentfusion: End-to-end differentiable reconstruction and rendering for unseen object pose estimation. In *Proceedings of the IEEE/CVF Conference on Computer Vision and Pattern Recognition*, pages 10710–10719, 2020. 1, 2, 3, 4, 6, 9
- [47] Sida Peng, Yuan Liu, Qixing Huang, Xiaowei Zhou, and Hujun Bao. Pvnnet: Pixel-wise voting network for 6dof pose estimation. In *Proceedings of the IEEE/CVF Conference on Computer Vision and Pattern Recognition*, pages 4561–4570, 2019. 3
- [48] Luis Pérez, Iñigo Rodríguez, Nuria Rodríguez, Rubén Usamentiaga, and Daniel F García. Robot guidance using machine vision techniques in industrial environments: A comparative review. *Sensors*, 16(3):335, 2016. 1
- [49] Mahdi Rad and Vincent Lepetit. Bb8: A scalable, accurate, robust to partial occlusion method for predicting the 3d poses of challenging objects without using depth. In *Proceedings of the IEEE international conference on computer vision*, pages 3828–3836, 2017. 3
- [50] René Ranftl, Alexey Bochkovskiy, and Vladlen Koltun. Vision transformers for dense prediction. In *Proceedings of the IEEE/CVF international conference on computer vision*, pages 12179–12188, 2021. 10
- [51] René Ranftl, Katrin Lasinger, David Hafner, Konrad Schindler, and Vladlen Koltun. Towards robust monocular depth estimation: Mixing datasets for zero-shot cross-dataset transfer. *IEEE transactions on pattern analysis and machine intelligence*, 44(3):1623–1637, 2020. 10
- [52] Tianhe Ren, Shilong Liu, Ailing Zeng, Jing Lin, Kunchang Li, He Cao, Jiayu Chen, Xinyu Huang, Yukang Chen, Feng Yan, Zhaoyang Zeng, Hao Zhang, Feng Li, Jie Yang, Hongyang Li, Qing Jiang, and Lei Zhang. Grounded sam: Assembling open-world models for diverse visual tasks, 2024. 3
- [53] Paul-Edouard Sarlin, Daniel DeTone, Tomasz Malisiewicz, and Andrew Rabinovich. Superglue: Learning feature matching with graph neural networks. In *Proceedings of the IEEE/CVF conference on computer vision and pattern recognition*, pages 4938–4947, 2020. 4
- [54] Ivan Shugurov, Fu Li, Benjamin Busam, and Slobodan Ilic. Osop: A multi-stage one shot object pose estimation framework. In *Proceedings of the IEEE/CVF Conference on Computer Vision and Pattern Recognition*, pages 6835–6844, 2022. 1, 2, 3
- [55] Yongzhi Su, Mahdi Saleh, Torben Fetzer, Jason Rambach, Nassir Navab, Benjamin Busam, Didier Stricker, and Federico Tombari. Zebrapose: Coarse to fine surface encoding for 6dof object pose estimation. In *Proceedings of the IEEE/CVF Conference on Computer Vision and Pattern Recognition*, pages 6738–6748, 2022. 3
- [56] Jiaming Sun, Zehong Shen, Yuang Wang, Hujun Bao, and Xiaowei Zhou. LoFTR: Detector-free local feature matching with transformers. *CVPR*, 2021. 2, 4, 6
- [57] Jiaming Sun, Zihao Wang, Siyu Zhang, Xingyi He, Hongcheng Zhao, Guofeng Zhang, and Xiaowei Zhou. Onepose: One-shot object pose estimation without cad models. In *Proceedings of the IEEE/CVF Conference on Computer Vision and Pattern Recognition*, pages 6825–6834, 2022. 1, 2, 3
- [58] David Joseph Tan, Federico Tombari, and Nassir Navab. Real-time accurate 3d head tracking and pose estimation with consumer rgb-d cameras. *International Journal of Computer Vision*, 126:158–183, 2018. 1
- [59] Bugra Tekin, Sudipta N Sinha, and Pascal Fua. Real-time seamless single shot 6d object pose prediction. In *Proceedings of the IEEE conference on computer vision and pattern recognition*, pages 292–301, 2018. 3
- [60] Meng Tian, Marcelo H Ang, and Gim Hee Lee. Shape prior deformation for categorical 6d object pose and size estimation. In *Computer Vision—ECCV 2020, : 16th European Conference, Glasgow, UK, August 23–28, 2020, Proceedings, Part XXI 16*, pages 530–546. Springer, 2020. 3
- [61] Shinji Umeyama. Least-squares estimation of transformation parameters between two point patterns. *IEEE Transactions on Pattern Analysis & Machine Intelligence*, 13(04):376–380, 1991. 3
- [62] Boyan Wan, Yifei Shi, and Kai Xu. Socs: Semantically-aware object coordinate space for category-level 6d object pose estimation under large shape variations. *arXiv preprint arXiv:2303.10346*, 2023. 3
- [63] Angtian Wang, Adam Kortylewski, and Alan Yuille. Nemo: Neural mesh models of contrastive features for robust 3d pose estimation. *arXiv preprint arXiv:2101.12378*, 2021. 1
- [64] Gu Wang, Fabian Manhardt, Federico Tombari, and Xiangyang Ji. Gdrnet: Geometry-guided direct regression network for monocular 6d object pose estimation. In *Proceedings of the IEEE/CVF Conference on Computer Vision and Pattern Recognition*, pages 16611–16621, 2021. 3
- [65] He Wang, Srinath Sridhar, Jingwei Huang, Julien Valentin, Shuran Song, and Leonidas J Guibas. Normalized object coordinate space for category-level 6d object pose and size estimation. In *Proceedings of the IEEE/CVF Conference on Computer Vision and Pattern Recognition*, pages 2642–2651, 2019. 3
- [66] Tianfu Wang, Guosheng Hu, and Hongguang Wang. Object pose estimation via the aggregation of diffusion features. *arXiv preprint arXiv:2403.18791*, 2024. 1
- [67] Bowen Wen, Jonathan Tremblay, Valts Blukis, Stephen Tyree, Thomas Müller, Alex Evans, Dieter Fox, Jan Kautz, and Stan Birchfield. Bundlesdf: Neural 6-dof tracking and 3d reconstruction of unknown objects. In *Proceedings of the IEEE/CVF Conference on Computer Vision and Pattern Recognition*, pages 606–617, 2023. 3
- [68] Bowen Wen, Wei Yang, Jan Kautz, and Stan Birchfield. Foundationpose: Unified 6d pose estimation and tracking of novel objects. *arXiv preprint arXiv:2312.08344*, 2023. 4
- [69] Yu Xiang, Tanner Schmidt, Venkatraman Narayanan, and Dieter Fox. Posecnn: A convolutional neural network for 6d object pose estimation in cluttered scenes. *arXiv preprint arXiv:1711.00199*, 2017. 2, 3, 6
- [70] Yan Xu, Kwan-Yee Lin, Guofeng Zhang, Xiaogang Wang, and Hongsheng Li. Rnnpose: Recurrent 6-dof object pose refinement with robust correspondence field estimation and pose optimization. In *Proceedings of the IEEE/CVF Conference on Computer Vision and Pattern Recognition*, pages 14880–14890, 2022. 3, 9
- [71] Heng Yang and Marco Pavone. Object pose estimation with statistical guarantees: Conformal keypoint detection and geometric uncertainty propagation. In *Proceedings of the IEEE/CVF Conference on Computer Vision and Pattern Recognition*, pages 8947–8958, 2023. 3
- [72] Lihe Yang, Bingyi Kang, Zilong Huang, Xiaogang Xu, Jiashi Feng, and Hengshuang Zhao. Depth anything: Unleashing the power of large-scale unlabeled data. *arXiv preprint arXiv:2401.10891*, 2024. 10
- [73] Sergey Zakharov, Ivan Shugurov, and Slobodan Ilic. Dpod: 6d pose object detector and refiner. In *Proceedings of the IEEE/CVF International Conference on Computer Vision*, pages 1941–1950, 2019. 3
- [74] Hansong Zhang and Kenneth E Hoff III. Fast backface culling using normal masks. In *Proceedings of the 1997 symposium on Interactive 3D graphics*, pages 103–ff, 1997. 6
- [75] Jason Y Zhang, Deva Ramanan, and Shubham Tulsiani. Relpose: Predicting probabilistic relative rotation for single objects in the wild. In *European Conference on Computer Vision*, pages 592–611. Springer, 2022. 1, 2, 4
- [76] Chen Zhao, Tong Zhang, Zheng Dang, and Mathieu Salzmann. Dvmnet: Computing relative pose for unseen objects beyond hypotheses. *arXiv preprint arXiv:2403.13683*, 2024. 1, 2, 4, 6, 7, 8
- [77] Chen Zhao, Tong Zhang, and Mathieu Salzmann. 3d-aware hypothesis & verification for generalizable relative object pose estimation. *arXiv preprint arXiv:2310.03534*, 2023. 1, 2, 4, 6, 7, 8
- [78] Hang Zhao, Orazio Gallo, Iuri Frosio, and Jan Kautz. Loss functions for image restoration with neural networks. *IEEE Transactions on computational imaging*, 3(1):47–57, 2016. 6
- [79] Xu Zhao, Wenchao Ding, Yongqi An, Yinglong Du, Tao Yu, Min Li, Ming Tang, and Jinqiao Wang. Fast segment anything, 2023. 3

Supplementary Material for the Paper: Towards Human-level 3D Relative Pose Estimation: Generalizable, Training-Free, with Single Reference

Yuan Gao*, Yajing Luo*, Junhong Wang, Kui Jia, Gui-Song Xia

We address the following issues in the supplementary material files:

- 1) Angle Error Distribution on LM-O in Sect. **S1**.
- 2) Experiments with imprecise input depth in Sect. **S2**.
- 3) Our results on the LineMOD [3], LM-O [1], and YCB-V [6] datasets w.r.t. **per object** in Sect. **S3**.
- 4) Qualitative Results on the LineMOD [3], LM-O [1], and YCB-V [6] datasets for all the methods in Sect. **S4**.
- 5) We also attached a **video** depicting the overview and the label/training-free refinement procedure of our method (i.e., the video version of Fig. 2 in the main text), as well as the qualitative results.

S1. ANGLE ERROR DISTRIBUTION ON THE LM-O DATASET.

Figure **S1** presents the angle error distribution (ranging from 0 to 180 degrees) for all the methods on the LM-O dataset. The statistics reveal that at lower angle error thresholds (e.g., for $t \leq 10, 20$ in $\text{Acc}@t^\circ$), our approach substantially outperforms both 3DAHV [8] and DVMNet [7].

S2. EXPERIMENTS WITH IMPRECISE INPUT DEPTH

As discussed in Sec. I.A (Applicability) in the main text, our method has the potential to use imprecise depth. We validate this on the LineMOD [3] dataset. Concretely, we simulate the imprecise depth by adding Gaussian noise $\mathcal{N}(0, \sigma)$ to the ground-truth depth map D_r , where σ is set to:

$$\sigma = \lambda * d, \quad d = \max(D_r) - \min(D_r), \quad (1)$$

where d is the maximal depth difference of the input sample.

We validate different λ 's with 0.001, 0.003, and 0.005 on the LineMOD [3] dataset, the results are shown in Table **S1**, which demonstrate the potential of integrating our method with an off-the-shelf generalizable depth estimator.

Y. Gao is with the School of Electronic Information, Wuhan University, Wuhan, China. E-mail: ethan.y.gao@gmail.com

Y. Luo and G.-S. Xia are with the School of Computer Science, Wuhan University, Wuhan, China. E-mails: {yajingluo, guisong.xia}@whu.edu.cn

J. Wang is with MoreFun Studio, Tencent Games, Tencent, Shenzhen, China. E-mails: junhongwang@tencent.com

K. Jia is with the School of Data Science, The Chinese University of Hong Kong, Shenzhen, China. E-mails: kuijia@cuhk.edu.cn

Corresponding authors: Gui-Song Xia, Yuan Gao.

* indicates equal contribution.

TABLE S1
EXPERIMENTS WITH IMPRECISE DEPTH ON LINEMOD.

Metrics	Mean Err↓	Acc@30°↑	Acc@15°↑	Acc@10°↑	Acc@5°↑
$\lambda = 0.005$	33.10	69.52	52.66	40.16	20.64
$\lambda = 0.003$	30.92	71.44	54.96	42.90	23.10
$\lambda = 0.001$	30.11	72.00	55.10	43.04	24.22
Ours	29.93	72.06	54.90	42.74	24.32

TABLE S2
OUR RESULTS ON THE LINEMOD DATASET W.R.T. PER OBJECT. THE OBJECTS WITH RED TEXT ARE THOSE USED FOR TESTING IN THE MAIN PAPER.

Object	Mean Err↓	Acc@30°↑	Acc@15°↑	Acc@10°↑	Acc@5°↑
ape	43.41	46.90	26.10	17.40	5.80
benchvise	17.79	87.30	75.60	64.60	42.10
camera	24.10	73.70	58.00	46.80	27.60
can	26.49	75.00	63.20	55.00	37.80
cat	33.90	68.00	52.20	40.20	22.00
driller	35.58	76.90	59.40	44.60	23.90
duck	38.30	54.40	29.30	17.50	6.00
eggbox	27.63	77.40	66.10	57.10	36.90
glue	46.35	55.30	38.20	28.00	13.70
holepuncher	26.25	76.50	64.30	52.30	26.80
iron	33.20	73.70	58.80	48.90	29.60
lamp	29.28	79.30	66.20	56.20	36.90
phone	25.82	80.80	64.60	50.20	27.30
average	31.39	71.17	55.54	44.52	25.88

S3. PER OBJECT RESULTS ON THE LINEMOD, LM-O, AND YCB-V DATASETS

We present our results w.r.t. per object of the full LineMOD [3], LM-O [1], and YCB-V [6] datasets in Tables **S2**, **S3**, and **S4**, respectively. The experimental settings are the same as those in the main text, i.e., Tables II-IV.

Tables **S2**, **S3**, and **S4** show that our method performs well on all the objects of the three datasets without training, further validating the strong zero-shot unseen-object generalize-ability of our label/training-free method.

S4. QUALITATIVE RESULTS ON THE LINEMOD, YCB-V, AND LM-O DATASETS

Qualitative results on the LineMOD [3], LM-O [1], and YCB-V [6] datasets are illustrated in Figs. **S2**, **S3**, and **S4**, respectively. The ground truth and predicted poses are visualized by axes and 3D bounding boxes.

As depicted in Figs. **S2**, **S3**, and **S4**, our method outperforms the state-of-the-art methods [2, 4, 5, 7, 8] qualitatively in all the three datasets.

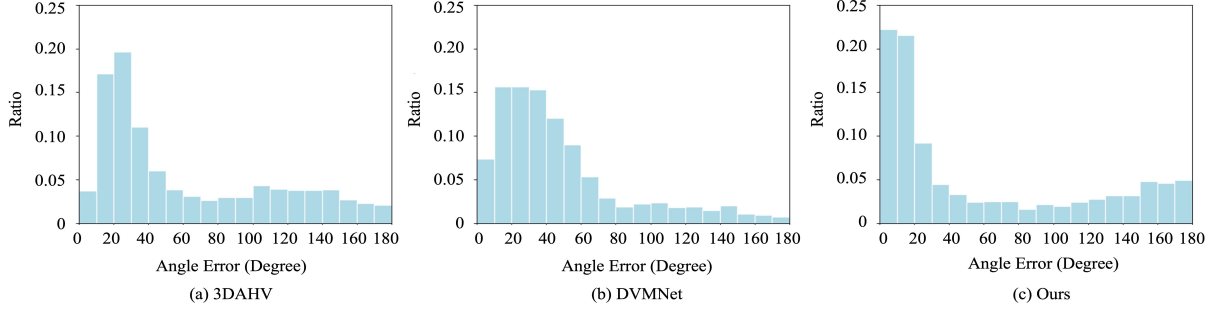


Fig. S1. Angle Error Distribution on LM-O.

TABLE S4

OUR RESULTS ON THE YCB-V DATASET W.R.T. PER OBJECT. THE OBJECTS WITH RED TEXT ARE THOSE USED FOR TESTING IN THE MAIN PAPER.

Object	Mean Err↓	Acc@30°↑	Acc@15°↑	Acc@10°↑	Acc@5°↑
002_master_chef_can	59.81	42.40	31.40	19.80	9.40
003_cracker_box	83.20	40.40	32.70	26.80	8.50
004_sugar_box	44.93	68.00	62.30	55.70	30.10
005_tomato_soup_can	61.65	36.50	25.80	19.70	9.40
006_mustard_bottle	20.76	86.40	83.30	77.80	59.70
007_tuna_fish_can	111.75	16.50	10.20	8.10	4.70
008_pudding_box	11.14	95.20	74.30	63.80	33.90
009_gelatin_box	8.13	99.50	87.20	78.30	32.40
010_potted_meat_can	99.01	26.80	22.30	13.20	4.60
011_banana	46.94	56.40	46.00	33.60	12.30
019_pitcher_base	33.43	58.60	41.40	28.50	9.50
021_bleach_cleanser	51.91	55.80	41.00	29.70	12.00
024_bowl	17.89	90.50	63.80	35.20	11.10
025_mug	43.98	40.80	22.90	15.50	3.30
035_power_drill	42.45	67.60	48.90	32.50	13.10
036_wood_block	39.52	69.10	48.50	30.50	10.50
037_scissors	27.55	83.50	60.00	41.10	15.40
040_large_marker	52.96	25.40	10.00	5.00	1.80
051_large_clamp	71.20	43.10	26.60	18.80	7.70
052_extra_large_clamp	88.61	27.00	14.90	7.40	2.80
061_foam_brick	27.89	81.90	73.00	50.10	13.30
average	49.74	57.69	44.12	32.91	14.55

TABLE S3

OUR RESULTS ON THE LM-O DATASET W.R.T. PER OBJECT. THE OBJECTS WITH RED TEXT ARE THOSE USED FOR TESTING IN THE MAIN PAPER.

Object	Mean Err↓	Acc@30°↑	Acc@15°↑	Acc@10°↑	Acc@5°↑
ape	60.85	42.10	22.40	11.60	2.10
can	38.49	63.60	53.10	41.70	19.60
cat	55.84	53.70	33.00	22.30	8.60
driller	52.29	59.10	42.20	28.50	7.30
duck	57.13	50.70	29.70	18.20	4.60
eggbox	45.94	58.90	43.40	34.50	16.00
glue	61.52	46.50	30.70	19.20	9.20
holepuncher	42.51	62.20	47.20	33.00	10.40
average	51.82	54.59	37.72	26.13	9.73

REFERENCES

[1] Eric Brachmann, Alexander Krull, Frank Michel, Stefan Gumhold, Jamie Shotton, and Carsten Rother. Learning 6d object pose estimation using 3d object coordinates. In *European conference on computer vision*, pages 536–551. Springer, 2014. 1

[2] Walter Goodwin, Sagar Vaze, Ioannis Havoutis, and Ingmar Posner. Zero-shot category-level object pose estimation. In *European Conference on Computer Vision*, pages 516–532. Springer, 2022. 1

[3] Stefan Hinterstoisser, Vincent Lepetit, Slobodan Ilic, Stefan Holzer, Gary Bradski, Kurt Konolige, and Nassir Navab. Model based training, detection and pose estimation of texture-less 3d objects in heavily cluttered scenes. In *Computer Vision-ACCV 2012: 11th Asian Conference on Computer Vision, Daejeon, Korea, November 5-9, 2012, Revised Selected*

Papers, Part I 11, pages 548–562. Springer, 2013. 1

[4] Amy Lin, Jason Y Zhang, Deva Ramanan, and Shubham Tulsiani. Relpose++: Recovering 6d poses from sparse-view observations. *arXiv preprint arXiv:2305.04926*, 2023. 1, 3

[5] Jiaming Sun, Zehong Shen, Yuang Wang, Hujun Bao, and Xiaowei Zhou. LoFTR: Detector-free local feature matching with transformers. *CVPR*, 2021. 1

[6] Yu Xiang, Tanner Schmidt, Venkatraman Narayanan, and Dieter Fox. Posecnn: A convolutional neural network for 6d object pose estimation in cluttered scenes. *arXiv preprint arXiv:1711.00199*, 2017. 1

[7] Chen Zhao, Tong Zhang, Zheng Dang, and Mathieu Salzmann. Dvmnet: Computing relative pose for unseen objects beyond hypotheses. *arXiv preprint arXiv:2403.13683*, 2024. 1

[8] Chen Zhao, Tong Zhang, and Mathieu Salzmann. 3d-aware hypothesis & verification for generalizable relative object pose estimation. *arXiv preprint arXiv:2310.03534*, 2023. 1, 3

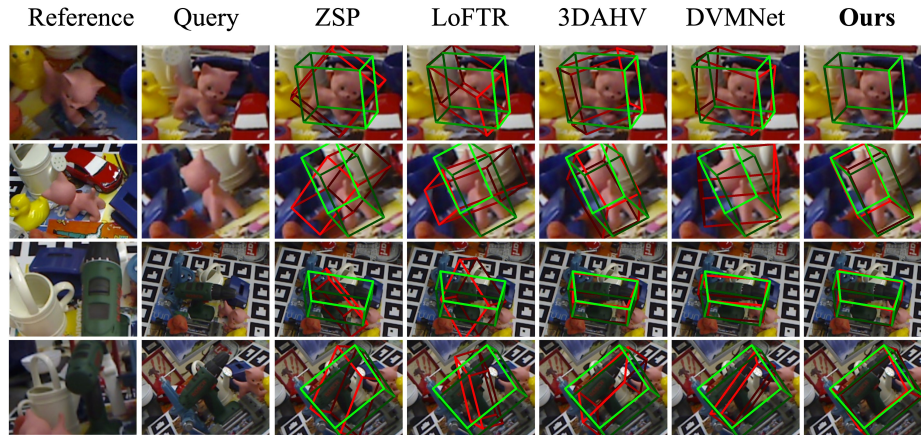


Fig. S2. **Qualitative results on LineMOD.** RelPose++ [4] did not release the LineMOD weights, the results of it in our main text were pasted from the 3DAHV paper [8], therefore the visualized results of RelPose++ are not included.

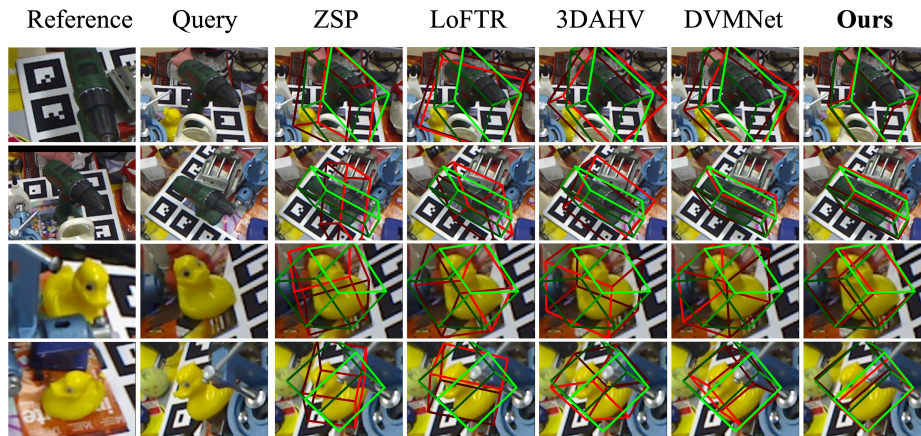


Fig. S3. **Qualitative results on LM-O.** LM-O is typically used solely to evaluate the models trained on LineMOD, since RelPose++ [4] have not released the LineMOD weights, the visualized results of RelPose++ are not included.

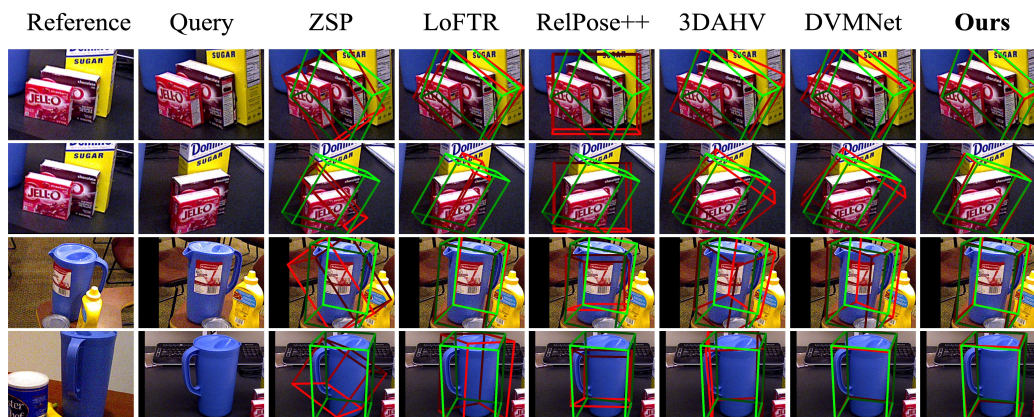


Fig. S4. **Qualitative results on YCB-V.** The predicted poses are visualized by red 3D bounding boxes while the ground truth poses are depicted by green 3D bounding boxes.